

Cite this: *Dalton Trans.*, 2017, **46**, 15769

Two-step hydrothermally synthesized carbon nanodots/WO₃ photocatalysts with enhanced photocatalytic performance†

Bo Song,^{a,b} Tingting Wang,^b Honggang Sun,^{*b} Qian Shao,^c Junkai Zhao,^c Kaikai Song,^b Luhan Hao,^d Li Wang^b and Zhanhu Guo  ^{*d}

In this study, carbon nanodots (C-dots)/WO₃ photocatalysts were prepared *via* a two-step hydrothermal method. The morphologies and optical properties of the as-prepared materials were investigated. Compared with the prepared WO₃ and C-dots, the C-dots/WO₃ possessed stronger photocatalytic capability and excellent recyclability for photocatalytic elimination of Rhodamine B. For example, the achieved first order reaction rate constant of 0.01942 min⁻¹ for C-dots/WO₃ was ~7.7 times higher than that of the prepared WO₃. The enhanced photocatalytic activity of C-dots/WO₃ was attributed to the enhanced light harvesting ability and efficient spatial separation of photo-excited electron–hole pairs resulting from the synergistic effect of WO₃ and C-dots. The high photocatalytic activity of C-dots/WO₃ remained unchanged even after 3 cycles of use. Meanwhile, a possible mechanism of C-dots/WO₃ for the enhanced photocatalytic activity was proposed.

Received 13th August 2017,
Accepted 12th October 2017

DOI: 10.1039/c7dt03003g

rsc.li/dalton

1. Introduction

Recently, environmental issues have aroused worldwide attention. Using the photocatalytic property of semiconductor oxides (such as TiO₂, ZnO, CeO₂ and WO₃) under solar radiation to deal with environmental pollutants has become an attractive and potential method.^{1–4} Among these visible active semiconductor photocatalysts, tungsten trioxide (WO₃, a band gap of 2.4–2.8 eV) is regarded as a promising catalyst due to its good response to the solar spectrum, high oxidizing ability of the holes in the valence band, low toxicity, and good stability.^{5–8} However, the photocatalytic activity of pure WO₃ is restricted by its high and fast electron–hole recombination rate and low reducing ability of the electrons in the conduction band. The enhanced photocatalytic activity of WO₃ has been explored with effective modification approaches.^{9,10} These strategies involve morphology and/or crystal phase control, metal/nonmetal elemental doping, noble metal/carbonaceous

material deposition, semiconductor coupling and composites.^{11–13} Among these, carbonaceous materials/WO₃ composites due to their unique structure and properties display a significantly improved photocatalytic activity. Enhanced photocatalytic activities have been demonstrated for WO₃/graphene and WO₃/carbon nanotube (CNT) composites. For example, Farhadian *et al.*¹⁴ prepared a WO₃/MWCNT nanocomposite for the degradation of naphthalene and found that the CNTs significantly enhanced the visible light photocatalytic capacity of WO₃ through high electrical conductivity of CNTs to reduce the electron–hole recombination rate. Khan *et al.*¹⁵ reported obviously improved photocatalytic properties of WO₃ nanorod/graphene with the high mobility of charge carriers and unique transport performance of graphene nanosheets.

Carbon nanodots (C-dots) as a zero-dimensional carbon-based nanomaterial possess fascinating physical and chemical properties such as a large specific surface area, non-toxicity, high aqueous solubility, photo-induced electron transfer, redox properties, luminescence, the quantum-confinement effect and physicochemical stability.^{16–19} C-Dots have been regarded as a viable alternative to traditional semiconductor quantum dots (QDs) in photocatalysis, photovoltaics, biosensing and optoelectronics.^{20,21} To date, C-dots have been successfully applied in conjunction with semiconductor nanoparticles (such as TiO₂, Ag₃PO₄ and Fe₂O₃) to improve their photocatalytic abilities in environmental and energy fields.^{22–26} The hybrid structures not only improve optical

^aMarine College, Shandong University, Weihai, 264209, Peoples R China^bSchool of Mechanical, Electrical & Information Engineering, Shandong University, Weihai, 264209, Peoples R China. E-mail: sunhg@sdu.edu.cn^cCollege of Chemical and Environmental Engineering, Shandong University of Science and Technology, Qingdao 266590, PR China^dIntegrated Composites Laboratory (ICL), Department of Chemical & Biomolecular Engineering, University of Tennessee, Knoxville, TN 37996, USA.

E-mail: zguo10@utk.edu

†Electronic supplementary information (ESI) available. See DOI: 10.1039/c7dt03003g

adsorption in the UV-visible region, but also suppress the recombination of photoexcited electron-hole pairs, thus enhancing the overall photocatalytic activity of the hybrid composite.^{27–30} The successful design of effective hybrid photocatalysts depends upon two facts: extending the adsorption over the entire solar spectrum by matching the band gap, and matching the conduction/valence band level of photocatalysts with the aid of the redox potentials of the photocatalytic reactions.^{31–34} Considering such outstanding performances of C-dots, the combination of C-dots and WO_3 may be regarded as an ideal strategy to construct an efficient and stable hybrid photocatalytic system. For example, Shi *et al.*³⁵ fabricated WO_3 nanoflakes decorated with carbon quantum dots (CQDs) *via* a seed-mediated solvothermal method in combination with subsequent impregnation-assembling. The as-prepared CQDs/ WO_3 nanocomposites showed an obviously more enhanced photocurrent than that of bare WO_3 for photoelectrochemical solar energy conversion. Zhang *et al.*³⁶ and Yang *et al.*³⁷ obtained carbon nanodots/ WO_3 nanorods Z-scheme composites through a combination of a hydrothermal method with subsequent surface deposition. The carbon nanodots/ WO_3 exhibited remarkably enhanced photocatalytic performance for the photodegradation of rhodamine B (Rh B) and phenol compared with pure WO_3 under UV, Vis or NIR irradiation. The preparation method plays a vital role in the photocatalytic activity of photocatalysts. The aforementioned methods to obtain C-dots/ WO_3 mainly are surface deposition which normally results in weak interfacial bonding between C-dots and WO_3 and thus limits the effective separation and transfer of photo-excited charges. Therefore, the exploration of a more effective preparation method for C-dots and WO_3 with strong interfacial bonding is imperative.

Herein, C-dots/ WO_3 hybrid composites were successfully prepared through a two-step hydrothermal method. The morphologies and crystalline structure of C-dots/ WO_3 were investigated by using SEM, TEM and XRD, respectively. The optical and electronic properties of C-dots/ WO_3 were examined by using FT-IR, Raman and UV-VIS diffuse reflectance spectra. Meanwhile, the photocatalytic property of the catalysts was evaluated by decomposing Rh B in aqueous solution under visible light irradiation. Remarkably, C-dots/ WO_3 hybrid photocatalysts exhibit enhanced photocatalytic activity and good reusability. The analysis of the photocurrent response and Nyquist plot confirms the effective separation and transport of photo-excited electrons-holes induced by C-dots that are responsible for the enhanced photocatalytic performance of the C-dots/ WO_3 . Furthermore, a possible mechanism for the enhanced photocatalytic activity of C-dots/ WO_3 was proposed.

2. Experimental

Ascorbic acid (A.R. 99%), ethanolamine (A.R. 99%), sodium tungstate dehydrate, $\text{Na}_2\text{WO}_4 \cdot 2\text{H}_2\text{O}$ (A.R. 99.5%), sodium chloride (A.R. 99.5%) and hydrochloric acid (A.R. 36–38%) were purchased from Aladdin Industrial Corporation (China).

Rhodamine B (Rh B) utilized in this work was obtained from Hangzhou Tiankai Co. Ltd (China). All the reagents were used as received without any further purification. Ultrapure water was used throughout the experimental process.

2.1 Synthesis of C-dots

C-dots were prepared through a hydrothermal method. First, 4.41 g ascorbic acid (AA) and 4.60 g ethanolamine (EN) were dissolved in ultrapure water (100 mL). Subsequently, the solution (100 mL) was transferred into a Teflon-lined autoclave, which was maintained at 476 K for 12 h. Then, the autoclave was cooled down to room temperature naturally. The prepared solution was further dialyzed with a dialysis bag (retained molecular weight: 1000) for 14 h and then freeze-dried. C-dots were obtained.

2.2 Synthesis of C-dots/ WO_3 and WO_3

Hybrid photocatalysts were fabricated by a hydrothermal method. Briefly, for a typical synthesis, 3.30 g $\text{Na}_2\text{WO}_4 \cdot 2\text{H}_2\text{O}$, 5.85 g NaCl, and different quantities of C-dots (0 mg, 5 mg, 10 mg, 15 mg, and 20 mg) were dissolved in 70 mL ultrapure water. The pH value of the solution was adjusted to about 0.65 by drop-wise addition of concentrated HCl solution under constant stirring. The obtained mixed solution was sealed in a 100 mL Teflon-lined stainless-steel autoclave, which was maintained at 453 K for 24 h. The resulting product was collected by centrifugation, rinsed with ultrapure water and ethanol, respectively, and dried at 333 K for 24 h. According to the amount of C-dots solution used in this experiment, the synthesized photo-catalysts were named WO_3 and C-dots/ WO_3 -X (X = 5, 10, 15, or 20), respectively. For comparison, pure WO_3 was obtained under the same experimental conditions in the absence of C-dots.

2.3 Characterization

X-ray diffraction (XRD) measurement was performed on a D8 Advanced X-ray diffractometer (Bruker Germany) using $\text{Cu K}\alpha$ radiation at a scan rate of $0.02^\circ/2\theta \text{ s}^{-1}$. High-resolution transmission electron microscopy (HRTEM) analysis was conducted on a JEM 2100 microscope with an accelerating voltage of 200 kV. Surface morphology was analyzed by using an S-4800 field emission SEM (FESEM, Hitachi, Japan) with an accelerating voltage of 5 kV. FT-IR spectra were obtained by using a VERTEX 80/80v FT-IR spectrometer. UV-VIS diffuse reflectance spectra were obtained by using a UV-VIS spectrophotometer (Shimadzu UV-2550, Japan). Raman spectra were obtained by using a Renishaw inVia Raman spectrometer with a 532 nm Ar ion laser. Photo-luminescence (PL) spectra were obtained by using a Hitachi F-4500 luminescence spectrophotometer at room temperature with an excited wavelength of 275 nm. Photo-electrochemical measurements and photocurrent curves were obtained using a standard three-electrode cell with an Ag/AgCl (3.0 M KCl) reference electrode and a platinum foil as a counter electrode on a CHI 660E electrode-chemical workstation. Na_2SO_4 (0.5 M) was used as the electrolyte solution. The working electrode was prepared by the spin coating method on

a 20 cm × 20 cm clean fluorine doped tin oxide (FTO). X-ray photoelectron spectroscopy (XPS) was conducted on an ESCALAB 250 spectrometer equipped with an Al K α source.

2.4 Photocatalytic experiments

The photocatalytic activity of the as-prepared hybrid photocatalysts was evaluated by decolorization of rhodamine B (Rh B) under visible light irradiation from a 300 W metal-halide lamp equipped with a 420 nm cut-off filter. 30 mg hybrid photocatalysts were dispersed into 100 mL Rh B (10 mg L⁻¹) aqueous solution, and continuously stirred in a completely dark environment for 60 min to ensure the absorption-desorption equilibrium between the photocatalyst and Rh B. An 8–10 mL mixed solution for dye concentration analysis was collected and centrifuged to remove the solid catalyst at 30 min intervals. The concentration change of Rh B was monitored by the optical absorption at 552 nm during the photoreaction process.

In the free radicals trapping experiments, four different scavengers were used for active oxidation species quenching (namely, sodium chromate(vi) (0.05 mM, Aladdin, 98%) for electrons, *p*-benzoquinone (BQ) (1 mM, Aladdin, 99%) for $\cdot\text{O}_2^-$, isopropanol (IPA) (0.5 mM, Aladdin) for $\cdot\text{OH}$ and ammonium oxalate (AO) (0.05 mM, Aladdin, 99%) for holes). The volume ratio of each scavenger and Rh B solution used in the experiment was 1 : 100. The scavengers were added into a 100 mL Rh B (10 mg L⁻¹) solution before photo-irradiation. The concentration of Rh B was measured at 30 min intervals.

3. Results and discussion

3.1 Crystal structure and morphology characterization

Fig. 1 shows a comparison of the XRD pattern for the as-prepared WO₃ and C-dots/WO₃-X materials. The hexagonal structure of WO₃ (JCPDS no. 35-1001) and the orthorhombic structure of WO₃·0.33H₂O (JCPDS no. 33-1387) are found in the as-prepared WO₃ and C-dots/WO₃.³⁸ The strong XRD diffraction peaks confirm that the WO₃ and C-dots/WO₃ possess high crystallinity. A significant phase transition can be found between the XRD patterns of WO₃ and C-dots/WO₃, demonstrating that C-dots have played an important role in the growth of WO₃ crystals. The introduction of C-dots has a negative effect on the formation of the hexagonal structure of WO₃ and this effect becomes gradually significant with increasing content of C-dots. Meanwhile, with the increase of C-dots content, the intensity of all diffraction peaks slightly declined resulting from the C-dots on the surface of WO₃ that obstructed the coherent scattering.³⁹

The TEM image indicates that the as-prepared C-dots possess an irregular spherical shape (Fig. S1[†]), while the HRTEM image of the C-dots shows a clear lattice fringe with a lattice spacing of 0.328 nm. This lattice fringe corresponds to the (002) crystal plane of graphitic carbon.³⁶ Furthermore, the particle size distribution of C-dots was also determined. As shown in Fig. S2,[†] the average diameter of C-dots was 10 nm

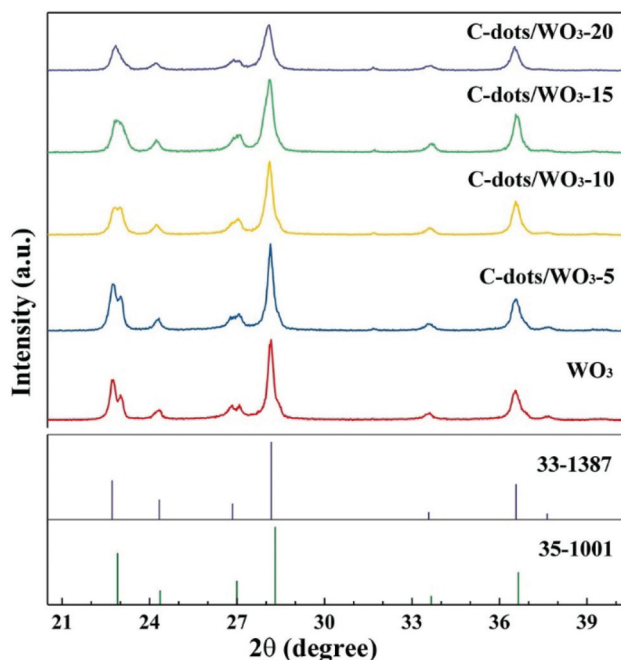


Fig. 1 XRD patterns of WO₃ and C-dots/WO₃-X.

with a particle size distribution from 6 to 14 nm. Fig. 2 shows the SEM images and digital photos of WO₃ ((a) and (b)) and C-dots/WO₃ ((c) and (d)). It can be noted that WO₃ (white powder) consists of a block-like body covered with granular particles, and the C-dots/WO₃ (black powder) mainly consists of a rod-like body with about 1 μm length. The color difference between WO₃ and C-dots/WO₃ testified that the C-dots were successfully generated on the surface of WO₃ *via* a two-step hydrothermal process. In order to further understand the microstructure of the C-dots/WO₃ hybrid material, the TEM images of C-dots/WO₃ with different scales are obtained (Fig. 3(a) and (b)). The C-dots with about 10 nm diameter are observed on the surface of rod-like WO₃. For the rod-like WO₃,

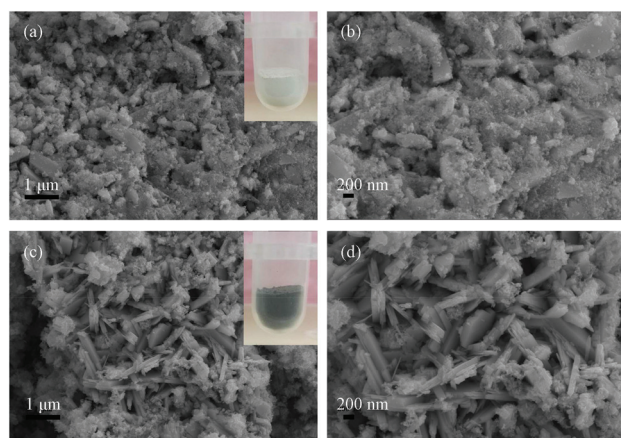


Fig. 2 SEM images of (a)/(b) WO₃ and (c)/(d) C-dots/WO₃. The inset in (a)/(c) shows the digital photos of WO₃ and C-dots/WO₃, respectively.

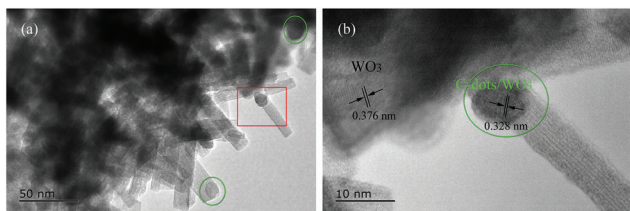


Fig. 3 TEM images of C-dots/WO₃: (a) low magnification and (b) high magnification.

the measured lattice fringe of 0.376 nm is due to the (020) interplanar spacing of WO₃.⁹ The crystalline lattice spacing of about 0.328 nm corresponds to the (002) crystal plane in the C-dots identification.³⁶ The lattice fringe spacing of some C-dots cannot be found as their quasi-spherical nanostructure possesses amorphous to nanocrystalline cores.

3.2 Spectrum analysis

FT-IR spectra are used to reveal the chemical bonds and functional groups on C-dots, WO₃, and C-dots/WO₃. As shown in Fig. 4(a), the absorption peaks of the C-dots at 3406, 2925–2866, 1631, 1436–1320 and 1046 cm⁻¹ correspond to the stretching vibration of O–H, CH_x, C=O, epoxy C–O and alcoxyl C–O bonds, respectively.³⁶ These peaks are also observed for graphene achieved by the Hummer method, indicating a similar microstructure between C-dots and graphene.³⁶ The characteristic peak of hydroxyl is still present for WO₃ at about 3500 cm⁻¹, which is mainly attributed to the absorbed and/or crystal water. The absorption peak of WO₃ at 1624 cm⁻¹ is associated with the stretching vibration of the W=O bond.¹³ Particularly, the broad absorption peaks of WO₃ at 600–900 cm⁻¹ originate from the stretching vibration of the W–O–W bond.³⁸ The spectrum of C-dots/WO₃ mainly presents the characteristic peaks of WO₃, which are due to the less C-dots content.

Raman spectra are utilized to analyze the structures of WO₃ and C-dots/WO₃. As shown in Fig. 4(b), the peak at 242 cm⁻¹ is attributed to the W–O–W bending vibration of bridging oxygen [$\delta(\text{W–O–W})$], while the peaks at about 680 and 806 cm⁻¹ are

considered to be from the stretching vibration of O–W–O [$\nu(\text{O–W–O})$].³⁸ The peak located at around 950 cm⁻¹ originates from the stretching mode of the terminal W=O bond, which is regarded as a typical peak of tungsten trioxide hydrates.²⁰ The position of the characteristic peaks of WO₃ is almost not affected by the introduction of C-dots. However, the intensity of characteristic peaks is weakened with increasing C-dots due to the influence of the fluorescence signal of C-dots.

Fig. 5 shows the UV-VIS diffuse reflectance spectra of the WO₃ and C-dots/WO₃ hybrid materials. The spectrum of WO₃ exhibits the fundamental absorption band in the UV region, and the absorption edge is approximately 420 nm.¹⁹ Remarkably, the C-dots/WO₃ showed a significant enhancement of light absorption at a wavelength of 400–500 nm due to C-dots absorbing visible light, and this light harvesting capability was enhanced with increasing C-dots content. The enhanced light absorption of the C-dots/WO₃ heterostructure results in more electron–hole pairs formed under irradiation and leads to an enhanced photocatalytic activity. Zhang *et al.*³⁶ also found that C-dots can endow the C-dots/WO₃ nanorods

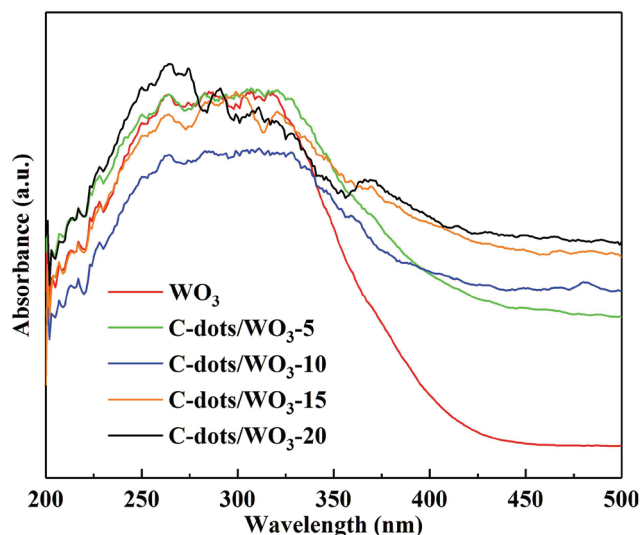


Fig. 5 UV-VIS diffuse reflectance spectra of the three samples.

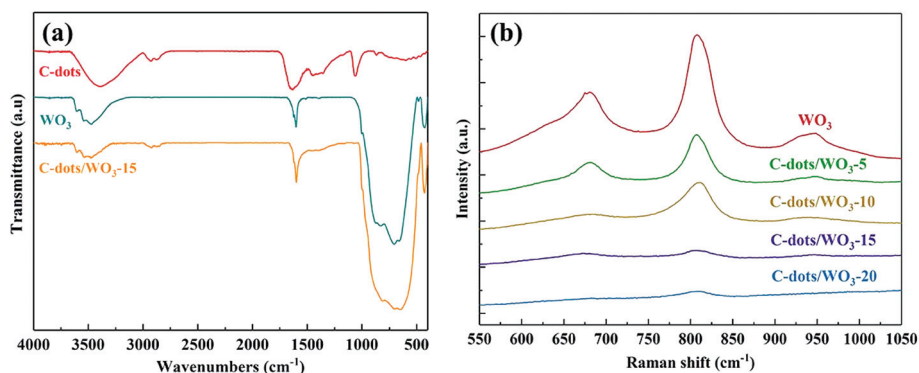


Fig. 4 FT-IR spectra and Raman spectra of WO₃ and C-dots/WO₃ photocatalysts.

with intense and wide adsorption across the UV-Vis region. The enhanced light-absorption capacity implies a more output of photo-excited electron-hole pairs. The optical band gap (E_g) of a semiconductor can be estimated from the classical Tauc approach.³⁵ As shown in Fig. S3,† the E_g values of pure WO_3 and C-dots/ WO_3 -15 were determined to be 2.75 and 2.71 eV, respectively. The small difference of E_g values between pure WO_3 and C-dots/ WO_3 -15 is related to the crystal structure of the materials.

Photocurrent measurement was carried out to evaluate the electron-hole recombination in the as-prepared samples. Fig. 6(a) displays the photocurrent-time ($I-t$) curves of WO_3 and C-dots/ WO_3 -15. It is noteworthy that the C-dots/ WO_3 -15 have a stronger photocurrent response than that of WO_3 . The photocurrent intensity of C-dots/ WO_3 -15 was ~ 3.2 times higher than that of pure WO_3 . This phenomenon suggests that the C-dots/ WO_3 hybrid material has a higher separation rate of photoexcited electrons-holes under visible light irradiation.³⁷ The C-dots as an excellent electron-acceptor can attract the photogenerated electrons on WO_3 , and thus inhibit the recombination of electrons and holes. Meanwhile, the electrode kinetics of the photocatalytic processes on the samples was evaluated by electrochemical impedance spectroscopy (EIS) (Fig. 6(b)). As shown in Fig. 6(b), one semicircle in the medium-frequency range is observed. This semicircle is ascribed to the charge transfer reaction between the electrode and electrolyte. The diameter of the semicircle in Nyquist plots is the embodiment of electrical resistance for charge transfer (R_{ct}) between the electrode and the electrolyte. An equivalent circuit (Fig. 6(b), inset) was used for fitting the electrochemical impedance spectra. The R_{ct} values of WO_3 and C-dots/ WO_3 -15 are calculated to be 1182.4 and 467.5 ohm, respectively. Compared with the Nyquist plot of WO_3 , the C-dots/ WO_3 -15 shows a remarkably decreased charge transfer resistance (R_{ct}), demonstrating that the introduction of C-dots improved the separation and transport efficiency of photogenerated electron-hole pairs.¹³ Based on the above experimental results, it is believed that the C-dots as excellent electron acceptors can reduce the probability of electrons-holes recombination,

which favors the photocatalytic activities of WO_3 by effective charge separation.^{8,12}

3.3 Photocatalytic activity of C-dots/ WO_3 nanocomposites

The photocatalytic activity of the as-prepared nanocatalysts was evaluated by the degradation of Rh B aqueous solutions. The relationship of the photodegradation rates with respect to time was investigated by using Langmuir-Hinshelwood models.¹⁶ The degradation rate equation can be expressed as eqn (1):

$$\frac{-dC}{dt} = \frac{k_{L-H}K_{ad}C}{1 + K_{ad}C'} \quad (1)$$

where K_{ad} is the adsorption coefficient of the photodegradation reaction, k_{L-H} is the reaction rate constant and C is the concentration of solution at a given time t .

$$\ln\left(\frac{C}{C_0}\right) = K_{ad}(C - C_0) + k_{L-H}K_{ad}t \quad (2)$$

where C_0 is the initial concentration of Rh B in aqueous solution. Because the $K_{ad}C$ is very small, the above equation can be simplified and integrated as:

$$\ln\left(\frac{C}{C_0}\right) = k_{L-H}K_{ad}t = kt \quad (3)$$

where $k = k_{L-H}K_{ad}$ is the first order reaction rate constant.

Fig. 7(a) illustrates the photocatalytic degradation performance of Rh B solution for C-dots/ WO_3 nanocomposites with different amounts of C-dots under visible light irradiation ($\lambda > 420$ nm). There is no photocatalytic degradation of Rh B in the absence of the catalyst, indicating that the photolysis of Rh B can be ignored. Meanwhile, WO_3 and C-dots both represent a limited photocatalytic activity in degrading the Rh B in solution. Although the C-dots possess a mass of functional groups on the surface, the C-dots display a limited absorption efficiency. This unsatisfactory absorption efficiency is attributed to the limited specific surface area due to the aggregation of C-dots.²⁸ It is interesting that these C-dots/ WO_3 photocata-

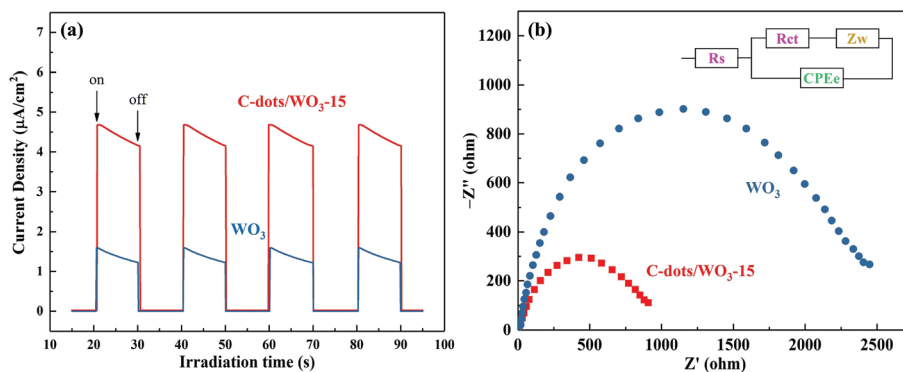


Fig. 6 Photocurrent responses (a) and Nyquist plots of electrochemical impedance (b) under visible light irradiation. Insert in (b) shows the corresponding equivalent circuit.

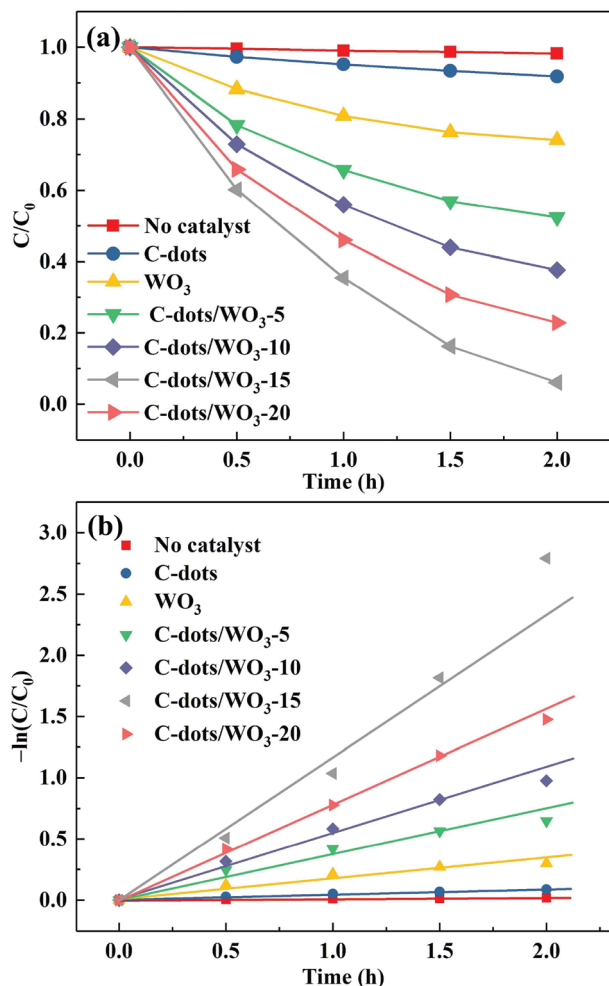


Fig. 7 Photocatalytic degradation of Rh B solution for WO_3 and C-dots/ WO_3 under visible light irradiation ($\lambda > 420$ nm).

lysts exhibit high photocatalytic activities under visible light illumination. The photocatalytic activities of C-dots/ WO_3 initially increase with increasing C-dots amount, but decrease when the C-dots amount reaches a higher level. For example, the Rh B removal efficiency of the C-dots/ WO_3 -15 was $\sim 94.4\%$ after 2 hour visible light irradiation, while the corresponding efficiencies of pure WO_3 and C-dots were 26.0% and 7.8%, respectively. Table 1 shows the amount of residual Rh B and the first order reaction rate constants of different photocatalysts. Fig. 7(b) shows the linear fitting curves between $-\ln(C/C_0)$ and reaction time, indicating the first order kinetic of the prepared photocatalysts. Through data comparison, it can be concluded that the C-dots significantly enhanced the photocatalytic activity of C-dots/ WO_3 . The first order reaction rate constant of 0.01942 min^{-1} was achieved in the presence of 15 mg C-dots, which was ~ 7.7 times higher than that of WO_3 .

3.4 Stability and reusability of C-dots/ WO_3 nanocomposites

The stability and reusability are vital to the practical applications of photocatalysts. Here, the stability and reusability of

Table 1 First order reaction rate constant of the prepared photocatalysts

Samples	Amount of residual Rh B after 2 h irradiation (%)	First order reaction rate constant (min)
No catalyst	0.9829	0.00015
C-Dots	0.9180	0.00072
WO_3	0.7407	0.00250
C-Dots/ WO_3 -5	0.5233	0.00625
C-Dots/ WO_3 -10	0.3766	0.00917
C-Dots/ WO_3 -15	0.0609	0.01942
C-Dots/ WO_3 -20	0.2285	0.01358

the as-prepared photocatalysts are assessed by recycled photodegradation experiment of Rh B solution. After each photodegradation cycle, the photocatalysts were collected according to the following procedures: rinsing with ultrapure water, centrifugation, and desiccation at 353 K for 7 hours. The residual photocatalysts were reused in the next photodegradation reaction, and the same amount of recollected C-dots/ WO_3 powders were used in the photodegradation reaction under the identical conditions. Fig. 8 shows the recyclability of C-dots/ WO_3 -15 in the photocatalytic decomposition of Rh B. The photocatalytic activity of C-dots/ WO_3 -15 remained constant after 3 cycles under the same conditions. From the results, it is clear that C-dots/ WO_3 -15 photocatalysts exhibited high stability and reusability for visible light degradation of Rh B solution, even after re-using the photocatalysts three times.

3.5 Photocatalytic mechanism

Photoluminescence (PL) spectra have an extensive application in the characterization of charge transfer, migration and recombination processes in photocatalysts.² A weaker intensity suggests a smaller recombination probability of electron-hole pairs.⁵ Fig. 9 shows the PL spectra of pure WO_3 and C-dots/ WO_3 hybrid materials. Both reveal an emission peak centered at around 470 nm. The significantly reduced intensity of this

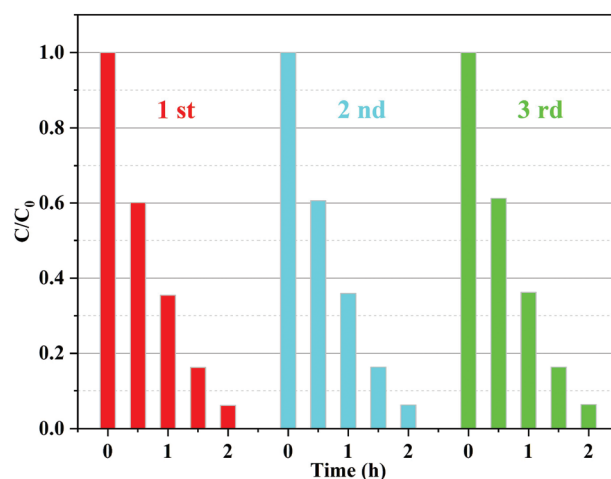


Fig. 8 Recycled degradation of Rh B solution for C-dots/ WO_3 -15 under visible light irradiation ($\lambda > 420$ nm).

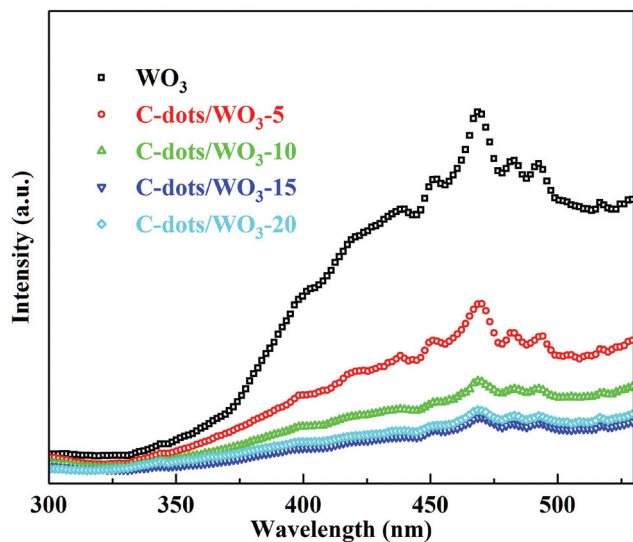


Fig. 9 Photoluminescence spectra of photocatalysts.

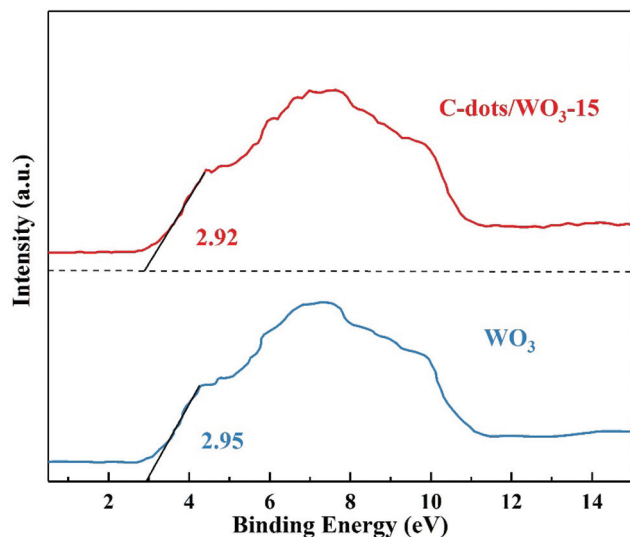


Fig. 10 XPS valence band spectrum.

emission band due to the C-dots anchored on the WO_3 surface indicates efficient transfer of the photoexcited electrons from WO_3 to C-dots. This agrees well with the experimental results of the photocatalytic test, which confirms that the C-dots successfully inhibit the recombination of electron-hole pairs and thus enhance the photocatalytic capability of WO_3 . Furthermore, the VB gaps (E_v) of the as-prepared samples were determined through the XPS valence band spectra. The E_v values of WO_3 and C-dots/ WO_3 -15 were calculated to be approximately 2.95 and 2.92 eV, respectively (Fig. 10). The corresponding CB gaps (E_c) of WO_3 and C-dots/ WO_3 -15 were estimated at 0.20 and 0.21 eV, respectively, according to $E_c = E_v - E_g$. As we all know, an appropriate band gap and the proper matching of the CB and VB levels are vital to the desired photocatalysts,^{1,7} and a relatively high CB gap is favorable to the formation of heterostructures and charge-carrier transport.⁹

Meanwhile, free radicals trapping experiment is used to reveal the roles of the main active oxidation species (AOSs) in the photocatalysis process over WO_3 and C-dots/ WO_3 -15 (Fig. 11).^{40,41} The AOSs (namely, e^- , $\cdot\text{O}_2^-$, $\cdot\text{OH}$ and h^+) were quenched using four different scavengers: sodium chromate, BQ, IPA and AO. As shown in Fig. 11(a), e^- and h^+ play the important role in the photocatalytic reaction of WO_3 , while $\cdot\text{OH}$ and $\cdot\text{O}_2^-$ were scarce. In the C-dots/ WO_3 -15 system (Fig. 11(b)), all four types of AOSs were found in the photocatalytic reaction. The influences of the scavengers on the reaction rate were in the order of AO (for h^+) > IPA (for h^+) > BQ (for $\cdot\text{O}_2^-$) > sodium chromate (for e^-). h^+ , $\cdot\text{OH}$ and $\cdot\text{O}_2^-$ made a major contribution to the photocatalytic degradation of Rh B, while the concentration of e^- was reduced significantly. The behaviors of these AOSs in the C-dots/ WO_3 -15 have been considered as a consequence of the fast electron transfer rate.³⁶ The fast electron transfer has a positive effect on the generation of $\cdot\text{OH}$ from both h^+ and $\cdot\text{O}_2^-$, which enhances the photo-degradation rate. Compared to the C-dots/ WO_3 -15 system, almost no $\cdot\text{OH}$ and $\cdot\text{O}_2^-$ were generated in the WO_3 system, indicating that pure WO_3 is not capable of generating these AOSs under visible light irradiation. The introduction of

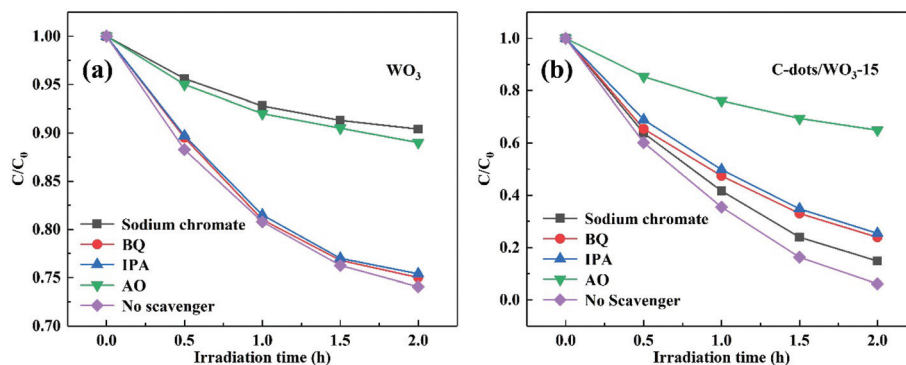


Fig. 11 Trapping experiment of active species during the photocatalytic degradation of Rh B over WO_3 and C-dots/ WO_3 -15 under visible light irradiation.

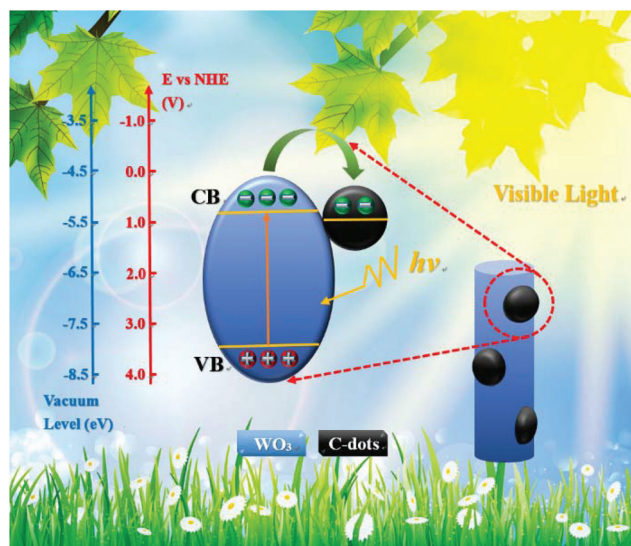


Fig. 12 Schematic illustration of the photodegradation mechanism of the C-dots/WO₃ nanocomposite.

C-dots favors the formation of $\cdot\text{OH}$ and $\cdot\text{O}_2^-$ in the C-dots/WO₃ system.

Fig. 12 illustrates the possible mechanism of C-dots/WO₃ for the photocatalytic degradation of Rh B under visible light irradiation. In this aqueous photocatalytic degradation system, the electrons (–) are delocalized from the conduction band (CB) to the valence band (VB) under visible light irradiation, and the holes (+) on the VB might react with the OH[–] in the water to form $\cdot\text{OH}$ radicals. The generated $\cdot\text{OH}$ radicals can initiate the oxidation degradation of Rh B later. Unfortunately, only a few delocalized electrons can take part in this oxidation degradation reaction due to the quick recombination between the delocalized electrons and holes on the VB. Thus, the efficient separation and transfer of photo-excited charge play a vital role in the photocatalytic activity of the catalyst. The appropriate integration between WO₃ and C-dots results in an efficient separation and transfer of photo-excited charge from WO₃ to C-dots. The C-dots act as the electron-acceptor to capture the delocalized electrons and hinder the recombination of the electrons and holes, which enhances the reaction probability of holes on the VB with the OH[–], and provides more $\cdot\text{OH}$ radicals for target degradation reaction. Meanwhile, the C-dots/WO₃ exhibits an enhanced light harvesting capacity, implying that more photo-excited electron–hole pairs were created under visible light irradiation. Therefore, the C-dots/WO₃ nanostructure shows superior photocatalytic activity compared to pure WO₃ under visible light irradiation.

4. Conclusions

Herein, C-dots/WO₃ hybrid materials have been prepared by a two-step hydrothermal method. The as-prepared C-dots/WO₃ possesses enhanced photocatalytic activity for the photodegra-

ation of Rh B under visible light irradiation compared with WO₃. Experimental analysis confirmed that C-dots not only play a vital role in the enhanced light-absorption capability of C-dots/WO₃, but also act as an electron acceptor to attract the electrons generated on WO₃, thus hindering the recombination of electron–hole pairs. The enhanced photocatalytic activity was attributed to two factors: enhanced light harvesting ability and effective separation of photo-excited electron–hole pairs. In addition, a possible photocatalytic mechanism for the photocatalytic reaction of C-dots/WO₃ was proposed. The combination of WO₃ and C-dots leads to an efficient separation and transfer of photo-excited charge from WO₃ to C-dots. C-Dots can act as an electron-acceptor to capture the delocalized electrons and hinder the recombination of the electrons and holes, which enhances the reaction probability of holes on the VB with the OH[–], and provides more $\cdot\text{OH}$ radicals for target degradation reaction. Besides, the introduction of C-dots endows C-dots/WO₃ with an enhanced light harvesting capacity, due to which more photo-excited electron–hole pairs were created under visible light irradiation. Meanwhile, this study provides a new strategy for the design and fabrication of high performance photocatalysts in the energy and environmental field.

Conflicts of interest

There are no conflicts to declare.

Acknowledgements

This work is financially supported by the National Natural Science Foundation of China (Grant No. 51603115 and 51402169) and the project funded by China Postdoctoral Science Foundation (Grant No. 2017M612266).

References

- (a) X. Bian, K. Hong, L. Liu and M. Xu, *Appl. Surf. Sci.*, 2013, **280**, 349–353; (b) X. Xiang, F. Pan and Y. Li, *Adv. Compos. Hybrid Mater.*, 2017, DOI: 10.1007/s42114-017-0001-6, in press.
- X. Chen, Y. Zhou, Q. Liu, Z. Li, J. Liu and Z. Zou, *ACS Appl. Mater. Interfaces*, 2012, **4**, 3372–3377.
- C. Dong, X. Xiao, G. Chen, H. Guan and Y. Wang, *Mater. Chem. Phys.*, 2015, **155**, 1–8.
- (a) J. Fang, H. Fan and G. Dong, *Mater. Lett.*, 2014, **120**, 147–150; (b) T. Wu, Q. Shao, S. Ge, L. Bao and Q. Liu, *RSC Adv.*, 2016, **63**, 58020–58027.
- W. Feng Yao, H. Wang, X. Hong Xu, X. Feng Cheng, J. Huang, S. Xia Shang, X. Na Yang and M. Wang, *Appl. Catal., A*, 2003, **243**, 185–190.
- (a) F. Wang and K. Zhang, *J. Mol. Catal. A: Chem.*, 2011, **345**, 101–107; (b) W. X. Zhu, S. S. Ge and Q. Shao, *RSC Adv.*, 2016, **85**, 81736–81743.

- 7 J. Xu, W. Wang, J. Wang and Y. Liang, *Appl. Surf. Sci.*, 2015, **349**, 529–537.
- 8 Z. Sun, L. Zhang, F. Dang, Y. Liu, Z. Fei, Q. Shao, H. Lin, J. Guo, L. Xiang, N. Yerra and Z. Guo, *CrystEngComm*, 2017, **19**, 3288–3298.
- 9 O. Arutanti, A. F. Arif, R. Balgis, T. Ogi, K. Okuyama and F. Iskandar, *AIChE J.*, 2016, **62**, 3864–3873.
- 10 S. Cao, C. Zhao, T. Han and L. Peng, *Mater. Lett.*, 2016, **169**, 17–20.
- 11 H. Chen, X. Xiong, L. Hao, X. Zhang and Y. Xu, *Appl. Surf. Sci.*, 2016, **389**, 491–495.
- 12 Z. DohleviL-MitroviL, S. StojadinoviL, L. Lozzi, S. AškrabiL, M. RosiL, N. TomiL, N. PaunoviL, S. LazoviL, M. G. NikoliL and S. Santucci, *Mater. Res. Bull.*, 2016, **83**, 217–224.
- 13 C. Dong, R. Eldawud, A. Wagner and C. Z. Dinu, *Appl. Catal., A*, 2016, **524**, 77–84.
- 14 M. Farhadian, P. Sangpour and G. Hosseinzadeh, *RSC Adv.*, 2016, **6**, 39063–39073.
- 15 M. E. Khan, M. M. Khan and M. H. Cho, *RSC Adv.*, 2016, **6**, 20824–20833.
- 16 X. Gu, F. Wu, B. Lei, J. Wang, Z. Chen, K. Xie, Y. Song, D. Sun, L. Sun, H. Zhou and F. Fang, *J. Power Sources*, 2016, **320**, 231–238.
- 17 Y. Zheng, Y. Zheng, S. Yang, Z. Guo, T. Zhang, H. Song and Q. Shao, *Green. Chem. Lett. Rev.*, 2017, **10**, 202–209.
- 18 F. Han, H. Li, L. Fu, J. Yang and Z. Liu, *Chem. Phys. Lett.*, 2016, **651**, 183–187.
- 19 Y. Kong, H. Sun, X. Zhao, B. Gao and W. Fan, *Appl. Catal., A*, 2015, **505**, 447–455.
- 20 S. Mohammed Harshulkhan, K. Janaki, G. Velraj, R. Sakthi Ganapthy and M. Nagarajan, *J. Mater. Sci.: Mater. Electron.*, 2016, **27**, 4744–4751.
- 21 Z. Liu, P. Li, Y. Dong, Q. Wan, F. Zhai, A. A. Volinsky and X. Qu, *Appl. Surf. Sci.*, 2017, **394**, 70–77.
- 22 C. Wang, Y. Wu, Y. Li, Q. Shao, X. Yan, C. Han, Z. Wang, Z. Liu and Z. Guo, *Polym. Adv. Technol.*, 2017, DOI: 10.1002/pat.4105, in press.
- 23 L. Zhang, W. Yu, C. Han, J. Guo, Q. Zhang, H. Xie, Q. Shao, Z. Sun and Z. Guo, *J. Electrochem. Soc.*, 2017, **164**(9), H651–H656.
- 24 M. E. Khan, M. M. Khan and M. H. Cho, *RSC Adv.*, 2016, **6**, 20824–20833.
- 25 Z. Ma, Y. L. Zhang, L. Wang, H. Ming, H. Li, X. Zhang, F. Wang, Y. Liu, Z. Kang and S. T. Lee, *ACS Appl. Mater. Interfaces*, 2013, **5**, 5080–5084.
- 26 H. Ming, Z. Ma, Y. Liu, K. Pan, H. Yu, F. Wang and Z. Kang, *Dalton Trans.*, 2012, **41**, 9526–9531.
- 27 J. Pan, Y. Sheng, J. Zhang, J. Wei, P. Huang, X. Zhang and B. Feng, *J. Mater. Chem. A*, 2014, **2**, 18082–18086.
- 28 S. Y. Park, H. U. Lee, Y. C. Lee, S. Choi, D. H. Cho, H. S. Kim, S. Bang, S. Seo, S. C. Lee, J. Won, B. C. Son, M. Yang and J. Lee, *Sci. Rep.*, 2015, **5**, 12420.
- 29 W. Yang, X. Wang, J. Li, X. Yan, S. Ge, S. Tadakamalla and Z. Guo, *Polym. Eng. Sci.*, 2017, DOI: 10.1002/pen.24675, in press.
- 30 J. Tian, Y. Leng, Z. Zhao, Y. Xia, Y. Sang, P. Hao, J. Zhan, M. Li and H. Liu, *Nano Energy*, 2015, **11**, 419–427.
- 31 Y. Yan, Q. Huang, C. Wei, S. Hu, H. Zhang, W. Zhang, W. Yang, P. Dong, M. Zhu and Z. Wang, *RSC Adv.*, 2016, **6**, 115317–115325.
- 32 P. Yang, J. Zhao, J. Wang, B. Cao, L. Li and Z. Zhu, *J. Mater. Chem. A*, 2015, **3**, 8256–8259.
- 33 H. Zhang, H. Huang, H. Ming, H. Li, L. Zhang, Y. Liu and Z. Kang, *J. Mater. Chem.*, 2012, **22**, 10501.
- 34 H. Zhang, H. Ming, S. Lian, H. Huang, H. Li, L. Zhang, Y. Liu, Z. Kang and S. T. Lee, *Dalton Trans.*, 2011, **40**, 10822–10825.
- 35 W. N. Shi, X. F. Zhang, J. Brillet, D. K. Huang, M. Li, M. K. Wang and Y. Shen, *Carbon*, 2016, **105**, 387–393.
- 36 J. Zhang, Y. Ma, Y. L. Du, H. Z. Jiang, D. D. Zhou and S. S. Dong, *Appl. Catal., B*, 2017, **209**, 253–264.
- 37 P. J. Yang, J. H. Zhao, J. Wang, B. Y. Cao, L. Li and Z. P. Zhu, *J. Mater. Chem. A*, 2015, **3**, 8256–8559.
- 38 Y. Q. Kong, H. G. Sun, X. Zhao, B. Y. Gao and W. L. Fan, *Appl. Catal., A*, 2015, **505**, 447–455.
- 39 J. Zhang, X. Y. Zhang, S. S. Dong, X. Zhou and S. S. Dong, *J. Photochem. Photobiol., A*, 2016, **325**, 104–110.
- 40 T. Liu, K. Yu, L. Gao, H. Chen, N. Wang, L. Hao, T. Li, H. He and Z. Guo, *J. Mater. Chem. A*, 2017, **5**, 17848–17855.
- 41 K. Zhang, G. Li, L. Feng, N. Wang, J. Guo, K. Sun, K. Yu, J. Zeng, T. Li, Z. Guo and M. Wang, *J. Mater. Chem. C*, 2017, **5**, 9359–9369.